Earth and Planetary Science Letters 385 (2014) 1–11

Contents lists available at ScienceDirect

Earth and Planetary Science Letters

www.elsevier.com/locate/epsl

Structure of the crust and the lithosphere beneath the southern Puna plateau from teleseismic receiver functions

B. Heit [a,*], M. Bianchi [a,h], X. Yuan [a], S.M. Kay [b], E. Sandvol [c], P. Kumar [a,d], R. Kind [a,e], R.N. Alonso [f], L.D. Brown [b], D. Comte [g]

[a] Deutsches GeoForschungsZentrum GFZ, Telegrafenberg, 14473 Potsdam, Germany
[b] Cornell University, EAS, Snee Hall, Ithaca, NY 14850, United States
[c] Department of Geological Sciences, University of Missouri, Columbia, MO 65211, United States
[d] NGRI, Hyderabad, India
[e] Freie Universität Berlin, Maltesserstr. 74-100, 12227 Berlin, Germany
[f] Universidad Nacional de Salta, Buenos Aires 177, 4400 Salta, Argentina
[g] Departamento de Geofisica, Universidad de Chile, Santiago, Chile
[h] Institute of Astronomy, Geophysics and Atmospheric Sciences, University of São Paulo, Rua do Matão 1226, 05508-090 São Paulo, SP, Brazil

ARTICLE INFO

Article history:
Received 5 July 2013
Received in revised form 6 October 2013
Accepted 9 October 2013
Available online 1 November 2013
Editor: P. Shearer

Keywords:
Central Andes
Puna plateau
teleseismic receiver functions
crustal thickness
lithosphere–asthenosphere boundary

ABSTRACT

We present a teleseismic P and S receiver function study using data from a temporary passive-source seismic array in the southernmost Puna plateau and adjacent regions. The P receiver function images show the distribution of crustal thickness and V_p/V_s ratio for this area. Over much of the southern Puna plateau, the crustal thickness is 50–55 km, whereas to the west a thicker crust (~60 to 75 km) is observed beneath much of the Andean volcanic arc region. From the Puna southward, there is little obvious change in the crustal thickness across the border of the plateau (south of 28°S). The crust is seen to progressively thin towards the east in the Pampean Ranges where it is 35–40 km thick. The southern Puna plateau is characterized overall by a low crustal V_p/V_s ratio (less than 1.70), implying a felsic crustal composition. An anomalously high V_p/V_s ratio of 1.87 is observed beneath the Cerro Galan volcanic center, in the region where a prominent crustal low-velocity zone identified below ~10 km depth probably extends into the lower crust. The crustal thickness determined under the Cerro Galan area (59 km) is close to that of the rest of the southern Puna. The prominent high V_p/V_s ratio and low-velocity zone beneath the Galan region implies the presence of a zone of partial melt or a magma chamber is consistent with hypothesis calling for lithospheric delamination beneath the Galan caldera. A widespread crustal low-velocity layer observed beneath much of the southern Puna, correlates well with crustal low-velocity anomalies observed by teleseismic tomography. The lithosphere–asthenosphere boundary beneath the array can be clearly observed by both P and S receiver functions at depths of 70–90 km in agreement with previous studies suggesting a thin lithosphere beneath the high elevated plateau. The mantle transition zone discontinuities appear at expected depths.

1. Introduction

The Altiplano–Puna region (marked as Puna in Fig. 1) in the Central Andes is a high elevated plateau that was formed in a subduction regime, which is flanked to the north and south by segments of flat subduction. The inherited plateau geological history, uplift, shortening and magmatism have been studied over the last decades (e.g., Cahill and Isacks, 1992; Allmendinger et al., 1997; Oncken et al., 2003; Kay and Coira, 2009 and references therein) and distinct differences have been recognized between the Altiplano to the north and the Puna to the south. In this paper we focus on the crustal and lithospheric structure beneath the southern end of the Puna plateau, until recently a geophysically poorly studied area. In a new study, Bianchi et al. (2013) gave an account of available geophysical information on the southern Puna plateau based on a number of studies, which began with the pioneering Magnetotelluric experiments of Febrer et al. (1982). To the south of 30°S, a number of seismic studies provide clues to the Moho, the lithosphere and the seismicity in the area located above the Chilean flat-slab region (e.g. Fromm et al., 2004; Alvarado et al. 2005, 2007; Gilbert et al., 2006; Gans et al., 2011; Porter et al., 2012, Ward et al., 2013).

The main features distinguishing the southern Puna plateau from the northern Puna and the Altiplano are: (a) a thinner continental lithosphere (Whitman et al., 1992; Heit et al., 2007), (b) the

* Corresponding author.
E-mail address: heit@gfz-potsdam.de (B. Heit).

0012-821X/$ – see front matter
http://dx.doi.org/10.1016/j.epsl.2013.10.017

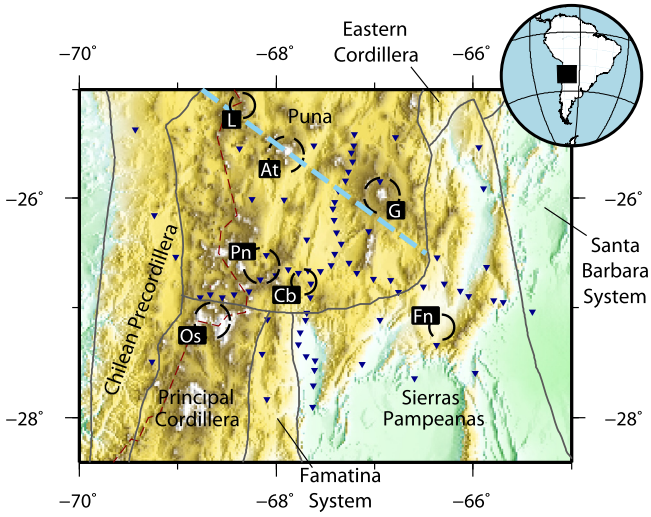

Fig. 1. Map showing the distribution of stations (blue inverted triangles) and the tectonic units (grey lines) in the southern Puna. Red triangles denote volcanoes. The red dashed line is the Chile/Argentina border. Volcanic centers inside the array are marked with black circles; At: Antofalla; G: Cerro Galan Caldera; Pn: Peinado; Cb: Cerro Blanco Caldera; Os: Ojos del Salado; Fn: Farallon Negro. The blue dashed line is the trace of the Archibarca lineament that runs from the northwest at the position of the Lastarria volcano (marked as L) to the southeast in the southern Puna plateau. (For interpretation of the references to color in this figure legend, the reader is referred to the web version of this article.)

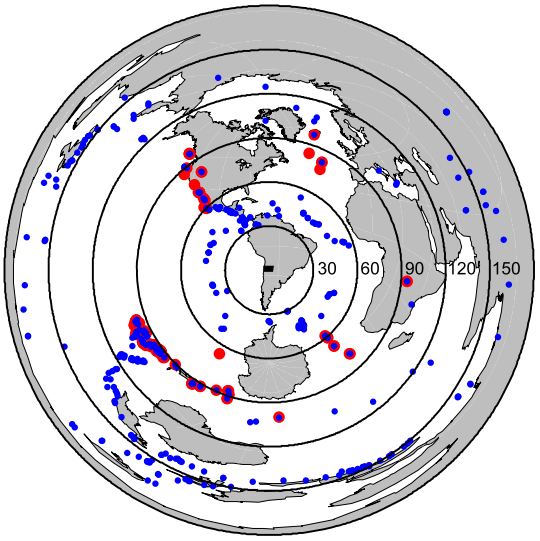

Fig. 2. Map of teleseismic earthquakes used in this study. Blue circles denote epicenters in a distance range of 30°–180° used for P and PP phases. Red circles denote earthquakes at epicentral distances between 60° and 115° used for S and SKS phases. Black concentric circles marked as reference for epicentral distances every 30°. (For interpretation of the references to color in this figure legend, the reader is referred to the web version of this article.)

subducting Nazca plate begins to shallow to the south (e.g., Cahill and Isacks, 1992; Mulcahy et al., submitted for publication) and (c) a distinctive sedimentary, magmatic and structural history (e.g. Coira et al., 1993; Kay et al., 1994, 1999; Allmendinger et al., 1997; Kay and Coira, 2009). Tectonically, the southern Puna has experienced less shortening than the Altiplano and the deformation is mainly concentrated in the eastern border of the plateau in the Eastern Cordillera and the Pampean Ranges (e.g., Kley and Monaldi, 1998; Kley et al., 1999). The large ignimbritic deposits in the area of the Cerro Galan caldera are suggested to be a consequence of piecemeal delamination of lithospheric material in the southern Puna (Kay and Kay, 1993; Kay et al. 1994, 2011).

Previous geophysical studies revealed low velocities in the crust and asthenosphere beneath the southern Puna plateau, suggesting higher temperatures than under the northern Puna and the Altiplano (e.g. Isacks, 1988; Whitman et al., 1992, 1996; Heit, 2005; Heit et al., 2007, 2008; Woelbern et al., 2009; Bianchi et al., 2013). The maximum crustal thickness along a profile at 25.5°S latitude obtained from a receiver function image, was nearly 60 km and the tomographic images show low-velocity anomalies in the crust that lessen into the mantle, consistent with asthenospheric material just below the Moho (Heit, 2005; Woelbern et al., 2009).

Here we apply the receiver function method to the teleseismic data recorded by the southern Puna passive-source seismic array, consisting of 74 stations (Fig. 1). In the analysis, we examine crustal thicknesses and intra-crustal layers with P receiver functions (PRF) and the lithosphere–asthenosphere boundary with S receiver functions (SRF).

2. Data and methodology

The seismic stations of the southern Puna array (Fig. 1) were distributed in two orthogonal profiles with a center at approximately 26.5°S and 67.5°W, which were surrounded by a sparser 2D array covering an area of approximately 300 × 300 km. For details concerning the station spacing and instrumentation see Bianchi et al. (2013). The data are archived at IRIS and GEOFON data centers.

We performed the teleseismic PRF receiver function analyses using events from the PDE catalog for which teleseismic P and PP phases were recorded at epicentral distances between 30° and 180° and for which magnitudes (mb) were greater than 5.5. For the SRF receiver function (including S and SKS phases), the epicentral distances were between 60° and 115° and magnitudes were greater than 5.5. The events used are shown in Fig. 2. The PRF computation was performed following the approach described by Yuan et al. (1997), whereas the SRF computation was performed using the approach by Kumar et al. (2006) and Yuan et al. (2006).

Seismograms with high signal/noise ratio have been visually inspected and manually selected for calculation of the P and S receiver functions. They were rotated, deconvolved and move out corrected for a constant reference slowness of 6.4 s/deg. The PRF were then divided into boxes according to piercing point locations at 60 km depth and stacked inside the boxed regions shown in Figs. 3 and 4 to enhance the signal-to-noise ratios of single traces (Dueker and Sheehan, 1997). We maximized the signal-to-noise ratios and homogenized the resolution based on the distribution of the stations in the array. We also enhanced coherent signals, like the Moho phase, at the same time that we suppressed random noise effects by stacking single traces from different events around stations in 0.5 × 0.5 deg boxes. Along the north–south and east–west profiles where the station spacing is about 10 km (Fig. 3), the boxes overlap by 0.1 deg. For the stations surrounding the two orthogonal profiles, similar sized boxes (i.e. 0.5 × 0.5 deg) do not overlap due to the larger station spacing (i.e. 50 km to 100 km; Fig. 4). In most cases, the Moho converted phase can be clearly recognized providing reliable estimates of the Moho depth.

Using the information provided by different crustal reverberations also known as Moho multiples, we estimated the Moho depth and the crustal V_p/V_s ratio following the H–K stacking approach (Zhu and Kanamori, 2000). The H–K stacks are done by boxes along the profiles north–south and west–east and by station piercing points elsewhere in the array since there are no overlaps where the station spacing is big. Some examples are presented in Fig. 5. Within each group a grid search is performed for estimates of Moho depth and crustal V_p/V_s ratio as indicated by the position of the maximum. The resulting V_p/V_s map shown in Fig. 6 illustrates the V_p/V_s variations in the region. Using the Moho depth values obtained by the H–K stacking method, we obtained a Moho depth map for the region (Fig. 7).

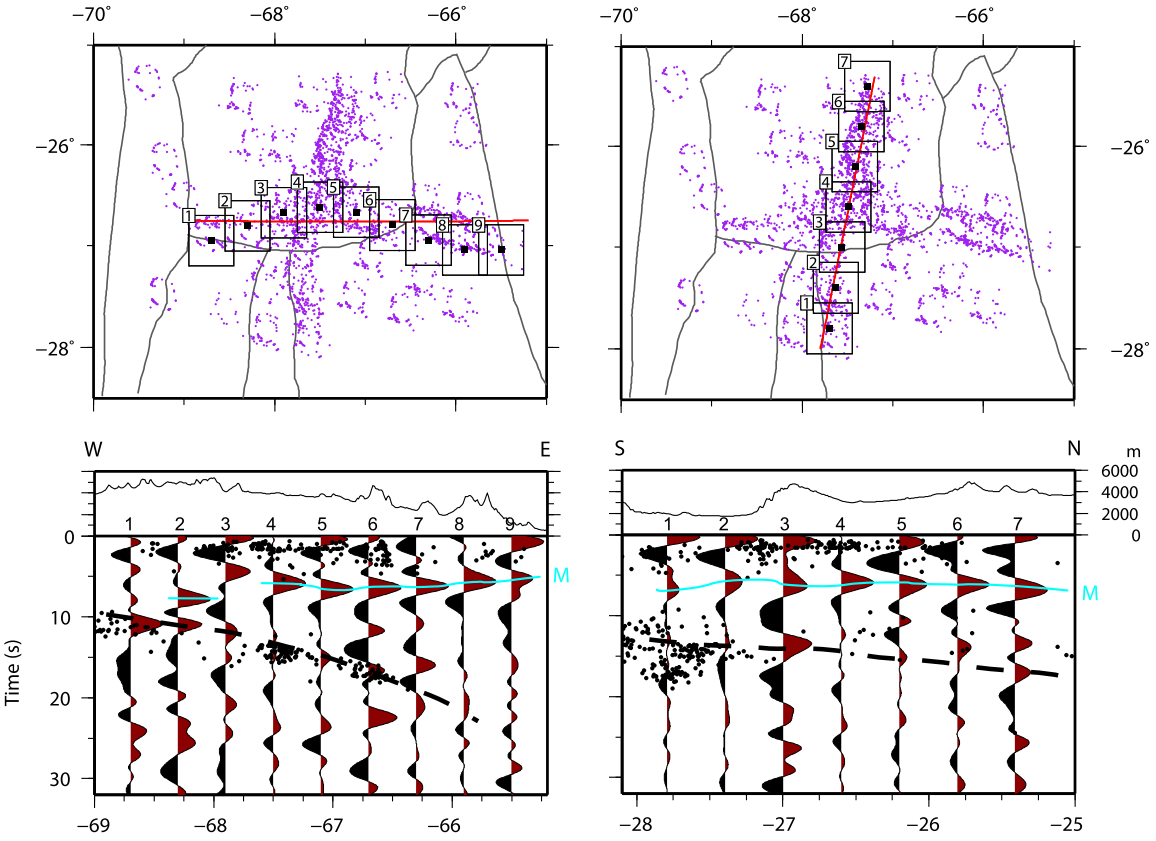

Fig. 3. Upper panels: Map showing the stacking boxes (black squares with bold squares in the center of each box) and piercing points (violet circles) for two orthogonal EW (left) and NS (right) profiles with the highest station density. The piercing points are calculated at a depth of 60 km, roughly representing the depth of the Moho. Receiver functions are stacked for piercing points falling into each box with a size of 0.5° overlapping by 0.1°. Lower panels: Stacked receiver functions along the two profiles. Positive amplitudes are shaded in red, negatives in black. Topography is sampled every 1 km across the red line on the maps. Black dots on the profiles are hypocenters from Mulcahy et al. (submitted for publication). The Moho phases are marked by the blue line and indicated as M on the profiles. (For interpretation of the references to color in this figure legend, the reader is referred to the web version of this article.)

3. Results

3.1. The Moho from P receiver functions

We present the PRF results in order to discuss the time arrivals of the Moho phase across the study area. As the station spacing is very close along the north–south and west–east profiles, we choose to stack the PRF along these lines to get an idea of the Moho time arrival variations across and along the strike of the subduction. In Fig. 3, we present the stacked traces per box for each profile that represents the Moho arrival times beneath the boxes along each profile. Along the west–east profile (26.8°S) the Moho phase (marked as M) is not clear at Box 1 but is well recognized in Box 2 at 7.9 s. If we consider this to be the Moho beneath the volcanic arc then we could also pick the small positive phase at 8.2 s to be the correct Moho phase in Box 1. The situation becomes more complicated for Box 3 at the position of the volcanic arc (∼68°W) where we detect the most prominent phase at 4.4 s not marked by the blue Moho line. This is an unexpected arrival time for the Moho-like phase as the traces from nearby boxes show clear later arrivals of the Moho, suggesting the phase at 4.4 s might be generated by a local feature. We suspect this phase to be an intra-crustal phase in an area where the Moho is invisible for receiver functions as we discuss below. In Box 4, the Moho phase is detected at 5.9 s while it arrives later at 6.5 s in Box 5 and then towards the east it arrives earlier where it can be seen at 6.3 s (Box 6), 6.1 s (Box 7), 5.7 s (Box 8) and finally 5.2 s in Box 9. The distribution of negative phases in the crust is well represented west of 66°W between Boxes 1–7 where they are found to arrive earlier beneath the volcanic arc at 2.5 s and at 3.2 s in the center of the plateau. The slab can be traced as a positive phase on the western side at 10.8 s (Boxes 1–2) and 11.6 s (Box 3). Eastward from Box 4, the slab should be around 30 s for Box 9 but it is for us impossible to determine its arrival time with our data. The earthquakes plotted in this figure (300 km swath from the line of every profile, i.e. 150 km to the north and 150 km to the south of the line) are located by Mulcahy et al. (submitted for publication) using the same network and have been used to improve the trace of the slab originally defined by Cahill and Isacks et al. (1992). We choose to plot a wide band of earthquakes to avoid assumptions of the position of the slab due to the scarcity of the slab seismicity. By plotting more events from the slab we expect the slab feature to become more stable (for more details about the slab geometry see Mulcahy et al., submitted for publication).

Along the South–North profile (67.8°W–67.2°W), it is possible to identify the Moho phases marked as M in Fig. 3. The Moho phase is identified at 6.7 s in Box 1 and arrives earlier at Box 2 (5.7 s). The Moho phase is then interpreted to arrive later in Box 3 (6.4 s) and it arrives progressively earlier towards the center of the profile at Boxes 4 and 5 (both at 5.9 s). At the northernmost end of the profile, the Moho phase arrival is identified at 7.0 s. In the crust, strong positive phases can be observed close to 0 s (followed by a negative phase) in Boxes 1 to 3. The continuity of these intra-crustal phases is then interrupted to the south where a break could be related to the tectonic border between the Puna to the north and the Pampean Block to the south in the region of the Fiambala basin as discussed later. To the north of Box 3, the presence of negative phases without any

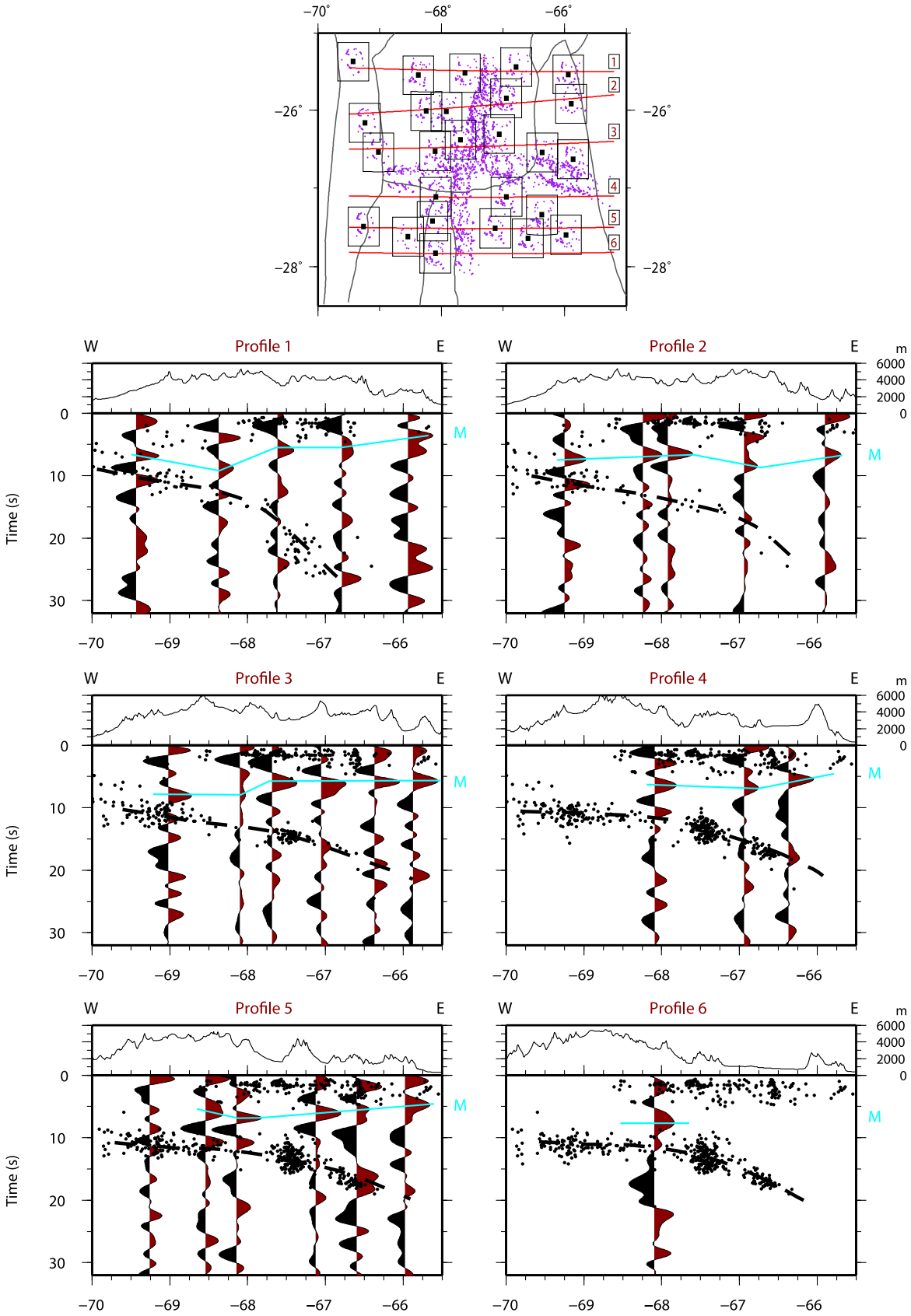

Fig. 4. Map of piercing points (upper panel) at a depth of 60 km grouped by boxes within which receiver functions are stacked and displayed along 6 profiles (marked as red lines on the upper panel map). Receiver functions shown in Fig. 3 are excluded here. Size of the boxes is the same as in Fig. 3. Black dots on the profiles denote hypocenters from Mulcahy et al. (submitted for publication). The Moho phases are marked by the blue line and indicated as M on the profiles. The black dashed line represents the approximate trace of the slab after Mulcahy et al. (submitted for publication). (For interpretation of the references to color in this figure legend, the reader is referred to the web version of this article.)

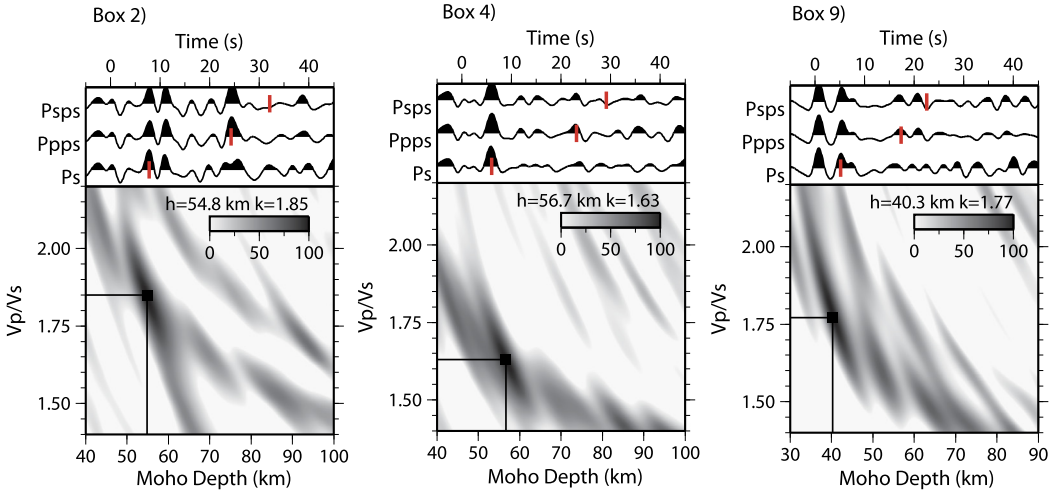

Fig. 5. Sample H–K stacks of receiver functions for three groups indicated in Fig. 3 (WE profile Boxes 2, 4, 9) and also shown in Fig. 6. Within each group a grid search is performed for estimates of Moho depth and crustal V_p/V_s ratio, indicated by the position of the maximum. The three traces on the right side of each panel are stacked receiver functions after moveout correction for the Ps, PpPs and PpSs phases, respectively. Red bars denote the predicted times of the three phases by the model obtained for each group. (For interpretation of the references to color in this figure legend, the reader is referred to the web version of this article.)

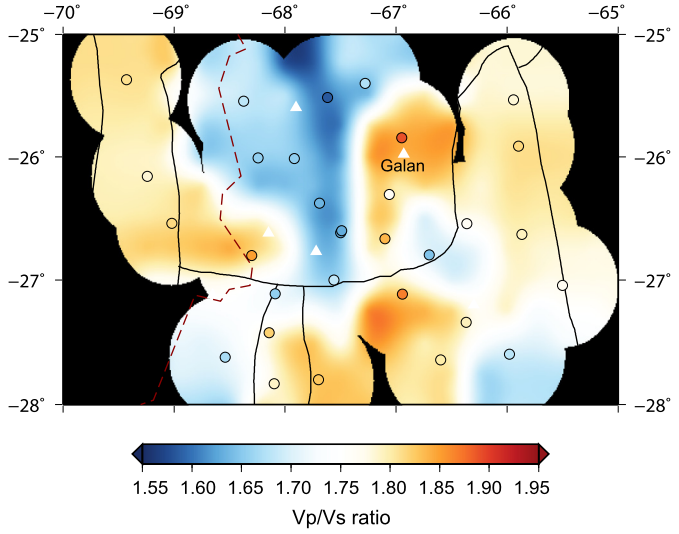

Fig. 6. Map of crustal V_p/V_s ratio determined by the H–K analysis (Zhu and Kanamori, 2000). The Ps Moho conversion and the crustal multiples (PpPs and PpSs) are used to determine the crustal thickness and V_p/V_s ratio. Black lines mark the tectonic units as shown in Fig. 1. The southern Puna is characterized by a low crustal V_p/V_s ratio (<1.70), indicating a felsic crustal composition. The V_p/V_s ratio beneath Cerro Galan is anomalously high (1.87), implying presence of melts. The position of Galan is included as a reference.

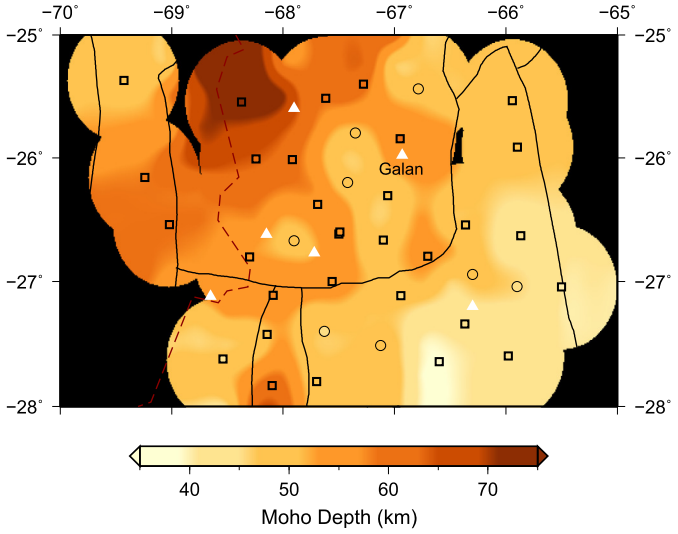

Fig. 7. Map of crustal thickness in the study area. Small circles represent the center of the boxes used to obtain the Moho depth. Most of the values are obtained by the H–K analysis (indicated by bold squares). For some of the boxes where the H–K analysis failed, an average V_p/V_s ratio of 1.74 is used to estimate the Moho depth (indicated by light circles). Black lines mark the tectonic units as in shown Fig. 1. The crust is thicker (>60 km) in the west and northwest beneath the volcanic arc. The Moho in the Puna region is relatively flat with depths varying between 50–60 km. To the southeast, the Sierras Pampeanas have a crustal thickness between 35–45 km. The position of Galan is included as a reference.

clear correlated positive phase close to 0 s is consistent with the distribution of low-velocity anomalies described in the crust by Bianchi et al. (2013) using a tomographic approach. The oceanic slab is not recognized along the profile in the area known as the Antofalla intermediate depth seismic gap in the subducted plate where sparsely distributed earthquakes (Cahill and Isacks, 1992; Mulcahy et al., submitted for publication) suggest a slab position at around 170 km depth in the north and 130 km depth in the south where the slab begins to shallow (110 km) into the flat-slab region at 29°S. The approximate position of the slab is marked based on the data of Mulcahy et al. (submitted for publication).

The results for the stations away from the W–E and S–N profiles are presented in Fig. 4, where the Moho phases are picked in different sections from North (Profile 1) to South (Profile 6). As in Fig. 3 the blue line marks the position of the Moho phase. As with most stations under the Puna in Fig. 3, the Moho phases arrive earlier than the Moho converted phases to the west beneath the volcanic arc. Beneath the Cerro Galan station we obtained a late arrival of the Moho phase at 8.7 s (Fig. 4, Profile 2 at 67°W). The Moho conversion times are observed earlier towards the eastern border of the plateau beneath the Sierras Pampeanas. The slab seismicity from Mulcahy et al. (submitted for publication) helps to infer the changing position of the subducted oceanic crust along the different profiles.

We use the Moho and its multiples to estimate the depth of the Moho and the crustal V_p/V_s ratio (Zhu and Kanamori, 2000). In Fig. 5, some examples of the H–K stacks of receiver functions are displayed. The boxes presented in Fig. 5 belong to profile that crosses the Puna plateau from west to east with a high number of stations with overlapping piercing points as can be seen in Fig. 3. Within each group, a grid search is performed for estimates of Moho depth and crustal V_p/V_s ratio which is indicated

by the position of the maximum amplitude. In each example we also show the stacked receiver functions moveout corrected for the Ps and the multiple phases (PpPs and PpSs), respectively. A good practice is that the phases are enhanced after the correct moveout correction and agree with the arrival times predicted by the final model. For some boxes the H–K stack does not give a reliable measurement, which is mostly due to the Moho multiples being too weak. In this case, we estimate the Moho depth by the arrival time of the Moho Ps phase using an average V_p/V_s ratio for the entire study area (1.74). The overall V_p/V_s map displayed in Fig. 6 shows a V_p/V_s ratio smaller than 1.7 beneath most of the southern Puna, whereas the region around Galan has a high value (1.87).

Fig. 7 displays the resultant Moho depth map where it is possible to observe a deep Moho in the northwest between 69°W and 68°W where the volcanic arc has a crustal thickness of 70 km. The Moho beneath the Puna plateau is seen to be relatively flat with depths varying between 50 km and 60 km. The Moho is shallower outside of the plateau where it can be observed between 35 km and 45 km in the Sierras Pampeanas (Pampean Ranges) to the south and east.

3.2. The crust beneath the Cerro Galan caldera

At the Cerro Galan station we obtained a late arrival of the Moho phase of 8.7 s (Fig. 4, Profile 2 at 67°W). This is an unexpected value (corresponding to a depth of 75 km using a V_p/V_s ratio of 1.74), because the Moho is relatively flat at a depth of ∼55 km beneath all nearby stations.

In Fig. 8, data from the station located inside the Galan caldera is presented for both P and S receiver function results. Due to bigger station separation little overlapping between data from neighboring stations is observed. In order to evaluate the results for the anomalously late Moho arrival beneath the Galan caldera, we present the individual PRF in Fig. 8a and compare them with the SRF (Fig. 8b). The Moho can be clearly identified in the PRF stack at 8.7 s, as well as in the individual traces. Although the quality and number of traces of the SRF do not compare to those of the PRF, the Moho phase clearly shows up in the SRF stack at 8.0 s, close to the Moho arrival in the PRF.

A strong negative phase can be identified in both datasets, arriving at 2.5 s in the PRF and at 3.5 s in the SRF. This is an indication of a pronounced low-velocity zone (LVZ) in the crust, that might account for the late arrivals of the Moho phases. Although the positions of the Moho and LVZ phases are similar in both methods, there are small differences in the arrival times, which can be explained by different piercing point locations of the PRF and SRF and lateral variations in the Moho depth and crustal heterogeneity, as well as different frequency contents of the P-to-S and S-to-P converted waves.

We performed waveform modeling of the P receiver functions for the Cerro Galan station (Fig. 9) by a linear inversion approach (Kind et al., 1995). It is well known that receiver function inversion is highly non-unique (Ammon, 1990). The final model obtained by a linear inversion tends to follow the start model, therefore, diverse nonlinear inversion approaches have been proposed (e.g., Sambridge, 1999). However, none of them are satisfied, due to the fact that the high-frequency receiver functions are sensitive to the seismic discontinuities, but do not constrain the absolute crustal velocity. Our receiver function modeling for the Cerro Galan station serves as a model check, rather than a unique inversion. We used fine layers with a layer thickness of 1 km and a strong smoothness control to avoid unrealistic velocity oscillation between neighboring layers. The waveform fitting is mainly applied for the crustal velocities, whereas a large damping factor is given to the uppermost mantle. A perfect waveform fitting could thus be hampered by the smoothness regularization. A strong crustal low-velocity zone is needed in the S wave velocity model in order to fit the strong negative phase detected at ∼2.5 s in the receiver function. In the model in Fig. 9, the Moho required to match the stacked P receiver function and the synthetic curve needs to be located at 55–60 km depth. By performing the H–K analysis, we obtain a Moho depth of 59 km and a crustal V_p/V_s ratio of 1.87 beneath the station. This implies that the Cerro Galan region has a crustal thickness in agreement with the thicknesses obtained across the southern Puna plateau and overlies a zone of melts in the crust that is seen in our data as a prominent low-velocity zone.

In the model in Fig. 9, the low-velocity zone begins at a depth of ∼10 km with a sharp velocity reduction and a further velocity reduction occurs at a depth of ∼20 km. Compared to the global reference IASP91 model the shear wave velocity remains low in almost the entire crust below 10 km depth with an elevated V_p/V_s ratio. The stepwise velocity reduction and the gradual nature of the Moho can explain the time difference of the PRF and SRF observations of the LVZ and Moho phases.

3.3. PRF and SRF migrated sections: the Moho and the LAB

We present the migrated sections incorporating all available data in Fig. 10. In addition to the Moho interface identified by the PRF, we look at the LAB discontinuity in order to answer the question, whether the Puna plateau has a thin lithosphere as suggested by the delamination hypothesis for this region (Kay and Kay, 1993; Kay et al., 1994). To better constrain the depth of the LAB, we also use the SRF method as it is better suited to investigate the upper mantle as has been successfully done in the Central Andes (Heit et al. 2007, 2008) and elsewhere (e.g., Li et al., 2004; Kumar et al., 2005, 2006; Sodoudi et al., 2006; Angus et al., 2006) as it is free of multiples. We used a single scatterer approach (Kind, et al., 2002) for the PRF and SRF migration. P-to-S and S-to-P converted amplitudes are back-projected to the space along the corresponding raypaths within a width of a Fresnel's zone. A 10×10 km smoothing window is applied over the migration sections. Ray-tracing is based on a 1D velocity model. Slightly dipping interfaces, such as the subducted slab in the present study with a dip angle $<15°$, can thus be properly reconstructed. For larger dips ($>30°$) a correction is necessary (Schneider et al., 2013).

The migrated PRF and SRF sections along the south–north and west–east profiles in Fig. 10 show clear images of the Moho and the LAB. The profiles incorporate data available in a 200 km wide swath on both margins of the profile and down to a depth of 200 km. The inclusion of data in the marginal swaths of the profile helps to increase the robustness of the results as the use of more events facilitates comparisons between the migrated sections and stacked traces in Figs. 3 and 4.

The west–east migrated sections in Fig. 10 clearly show the Moho topography (marked as M) in both the PRF and SRF profiles. The Moho is at depths near 45 km in the east beneath the Pampean Range, near 75 km in the west beneath the volcanic arc and near 50–60 km beneath the Puna plateau. Although in detail, the Moho appears to be at slightly different depths in the PRF and the SRF profiles, the depth trend is similar in both profiles and is in agreement with the result of the H–K analysis (Fig. 7). The negative phases (blue) below the Moho represent the lithosphere–asthenosphere boundary (marked LAB) which can be identified at similar depths between 70 km and 80 km in the PRF and SRF sections. The trace of the slab is recognized in the PRF section where the positive phase in red is coincident with the local seismicity detected by our network (Mulcahy et al., submitted for publication). The dispersion of the earthquake hypocenters on the profile is in part due to the north to south change in depth to the Wadati–Benioff zone across the array. A cluster of negative amplitudes at depth of ∼150 km below the earthquakes in the PRF profile, which

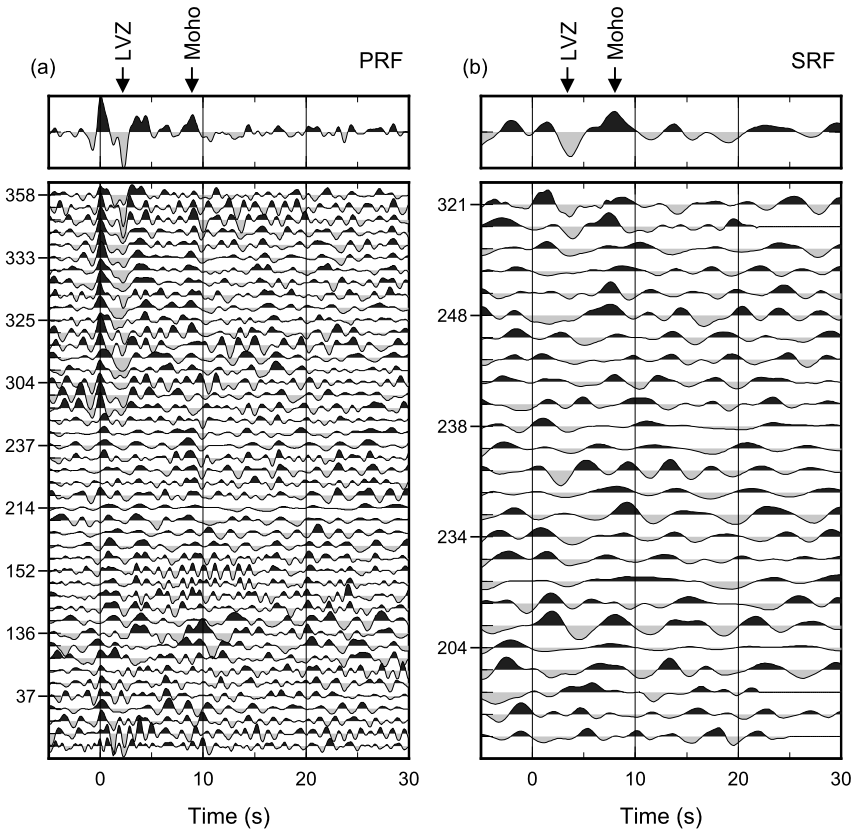

Fig. 8. P (a) and S (b) receiver functions for the station located at the Cerro Galan caldera. Individual receiver functions are sorted by back azimuth and displayed equally spaced. Sample back azimuth every 5 traces are indicated on the left side of each panel. Summation traces are displayed in the top panels. Positive amplitude is shaded in black, negative in gray. Two coherent conversion phases, the positive Moho conversion and a negative crustal conversion (LVZ), are indicated on the top of the summation traces. Both negative LVZ phases can be clearly observed by the P and the S receiver functions.

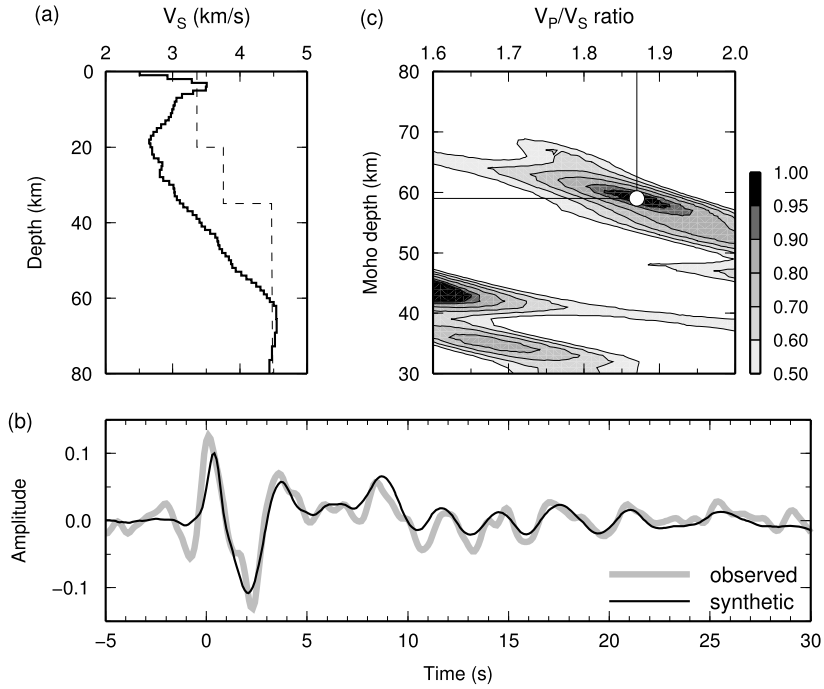

Fig. 9. Waveform modeling of P receiver functions for the Cerro Galan station. (a) S wave velocity model obtained by waveform fitting. A prominent crustal low-velocity zone is needed to fit the strong negative phase at ∼2.5 s in the receiver function shown in (b). In the model, the Moho is a gradient zone from 55 to 60 km depth. The dashed line is the global reference IASP91 model. (b) Stacked P receiver function (gray curve) and the synthetic one (black curve) corresponding to the model shown in (a). (c) H–K analysis showing a Moho depth of 59 km and a crustal V_p/V_s ratio of 1.87 beneath the station.

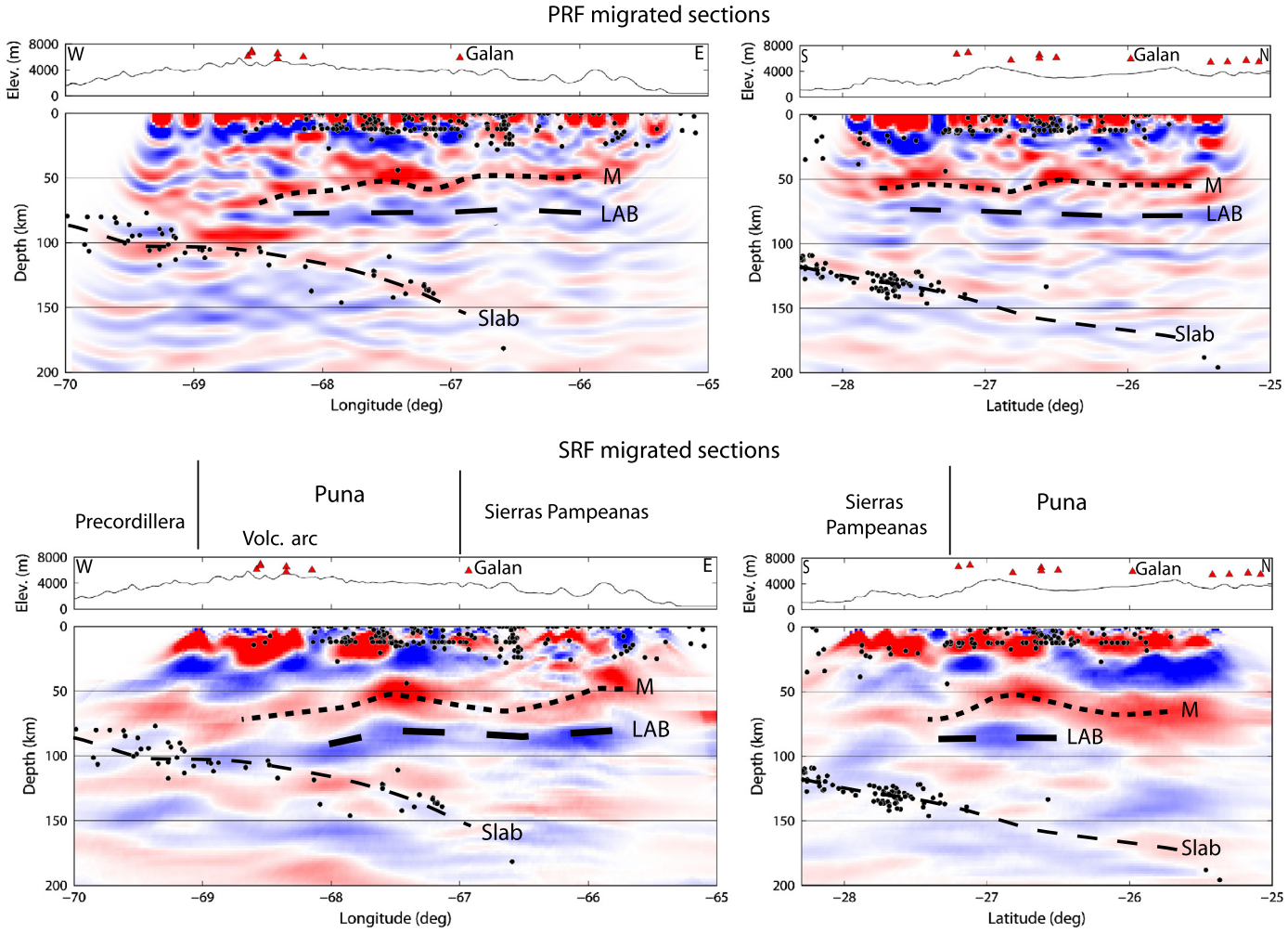

Fig. 10. Migrated sections performed using receiver functions with piercing points falling within a 100 km wide band along the profiles defined in Fig. 3. The upper two panels are west–east (left) and north–south (right) sections of P receiver functions. The lower panels are the corresponding S receiver function sections. Positive amplitudes are coded in red, while negative are coded in blue. Along all profiles the positive Moho phase (50–75 km) and the negative LAB phase (70–90 km) can be observed. Earthquakes from Mulcahy et al. (submitted for publication) within a same swath width along the profiles. The approximate position of the slab is marked by the dashed line. (For interpretation of the references to color in this figure legend, the reader is referred to the web version of this article.)

are also observed in the SRF section, may represent the base of the oceanic lithosphere. The positive slab converter is not as clear in the SRF profile. The thickness of the subducted Nazca lithosphere can be estimated to be about 50 km.

The PRF migrated section for the north–south profile clearly shows the Moho depth variations. The Moho is seen at 55 km in the north and deepens around 27°S at the southern border of the Puna plateau. In contrast, the SRF migrated section shows the position of the Moho phases to be deeper in the north (60 km) and to shallow to 55 km at the southern end of the Puna plateau at 27°S. This discrepancy in Moho topography in the north–south PRF and SRF profiles could be due to the strong low-velocity anomalies observed in the crust. A negative phase above the Moho in the middle crust can be traced along the PRF profile north of 28°S. An intra-crustal negative phase is even more clearly observed on the SRF profile north of 27°S where its presence coincides with the Puna plateau and the presence of the Sierras Pampeanas block south of 27°S. This low-velocity zone as explained above (see the Cerro Galan section) might produce the observed effect on the Moho, making it apparently to appear at greater depth. The PRF profile shows a clear negative phase at greater depth beneath the Moho that we interpret as the LAB. On the SRF profile, the LAB is only observed at 27°S (80 km) probably due to the low quality of the SRF. The down-going slab is not clearly observed in either the PRF or the SRF sections, although its position can be inferred when correlated with the sparse seismicity (see Mulcahy et al. for more details). The slab is difficult to image in this area where there is a pause in seismicity in the down-going slab. This is known as the Antofalla seismicity gap and our results are suggesting and supporting the idea of a hot mantle and crust beneath the southern Puna. This could be related with recent lithospheric delamination beneath the region.

4. Discussion

The small differences in depth determinations of the Moho and LAB between the results from the PRF and SRF analysis can be explained partly by different locations of P-to-S and S-to-P piercing points and partly by different frequency contents of the PRF and SRF. Specifically, the P-to-S conversions are closer to the stations whereas the S-to-P conversions sample areas farther away from the stations. The PRF has higher frequency content, therefore, is sensitive to sharper velocity contrast, whereas the SRF is more sensitive to gradual interfaces. The PRF could be affected by numerous crustal multiples that can mask the position of primary converted phases. The LAB is thus best resolved by the SRF as the profiles are free of disturbing multiples. The SRF is, however, noisier than the PRF, because the number of teleseismic events useful

for calculation of the SRF is limited for South America (Kind et al., 2012). For this reason, the use of SKS arrivals is imperative as demonstrated by Kind et al. (2012).

The data provided by all stations represent well constrained results for Moho depths that correspond to the different morphostructural units and major volcanic centers in the southern Puna plateau (Fig. 7). The Moho is deepest beneath the volcanic arc on the west where it reaches a depth of 75 km in the northwest of the array. Such a thick crust can be explained by large amounts of magmatic addition in combination with ductile thickening of the lower crust in response to crustal shortening (e.g. Isacks, 1988; Allmendinger et al., 1997; Oncken et al., 2003) with the resultant isostatic response leading to high topography. The thick crust is observed northwest of the Antofalla volcano in an area where some active volcanoes are located (i.e. Lastarria, see Fig. 1). The position of this thickened crust beneath the volcanic arc speaks for magmatic addition at the base of the crust. The Lastarria and nearby volcanoes are located at the western end of the Archibarca lineament (see Fig. 1) which runs through the Antofalla and Galan volcanoes in the northern edge of the southern Puna plateau. The Archibarca lineament is part of number of northwest–southeast trending fault systems considered to be zones of lithospheric weakness (e.g. Bianchi et al., 2013). The center of the Puna plateau shows a relatively thin crust with a Moho depth generally between 50 and 55 km. This is very thin compared to the Moho depth obtained beneath the volcanic arc. On average the crust beneath the southern Puna is 5–10 km thinner than that beneath the northern Puna and 20 km thinner than beneath the Altiplano (Yuan et al., 2002; Woelbern et al., 2009). Towards the eastern border of the Puna plateau (at 67°W) the crust is slightly thicker than the central part of the plateau what could be indicating that the thickening is related to shortening of the crust at the border between the Puna and the Pampean Ranges.

A receiver function Moho under the volcanic arc in the W–E profile in Box 3 on Fig. 3 appears to be invisible in the same locality that a strong P-to-S converted phase in Box 3 provides evidence for a strong interface at a depth near 35 km. A Moho at ∼35 km in this region is clearly inconsistent with the Moho depths in the migrated PRF section (Fig. 10) for the region, which show a crustal thickness near 70 km. An explanation for the lack of a clear Moho phase at the base of the crust and a strong intra-crustal discontinuity at this depth in the Box 3 profile is, however, consistent with eclogitization of the lower crust. Such a proposal for detecting the presence of eclogite in the lower crust by RFs was made by Gilbert et al. (2006) in the high cordillera region in the flat-slab region just to the south. In detail, they argued that an intra-continental discontinuity marking the top of eclogitized lower crust would create a larger impedance contrast than the boundary between the base of eclogitized lower crust and the mantle. This would lead to a situation in which the Moho interface would be nearly invisible to RFs due to the similarities of velocities of the mantle and the eclogitic lower crust. Such an explanation for the crust of the cordillera in the flat-slab region was noted to be consistent with previous inferences for the presence of an eclogitized crust based on geochemical data from Neogene lavas (e.g., Kay et al., 1987; Kay and Mpodozis, 2002). A similar argument can be made to explain the seismic observations in Box 3 under the volcanic arc on Fig. 3, which is the region where the crust might be expected to be the thickest. As in the flat-slab segment, eclogitization of the crust can be inferred to be related to magmatic addition in conjunction with ductile shortening of the lower crust in response to crustal shortening. In parallel with the flat-slab region, Kay and Coira (2009) have proposed that the peak of crustal thickening in this region could have accompanied the Miocene shallowing of the subducting Nazca plate under the southern Puna, which was followed by resteepening.

Recently, Carbonell et al. (2013) suggested that a geophysically invisible Moho might be an indication of a thick crust–mantle transition zone where the impedance changes very slowly between values for the crust to values of the mantle. They claim that this situation could be directly related to a fast tectonic crustal thickening due to a continental orogenesis which can be the case in the Central Andes.

The southern Puna plateau is characterized by low V_p/V_s ratios (less than 1.7), similar to the Bolivian Altiplano to the north where Zandt et al. (1994) reported a V_p/V_s ratio of 1.6. Beck and Zandt (2002) also obtained similar results for the Altiplano plateau (1.7) and suggested a felsic crust is responsible for this value.

A low-velocity crust with a high V_p/V_s ratio of 1.87 is observed in the crust beneath the Cerro Galan caldera (Fig. 6), consistent with a zone of partial melt under the region. This interpretation is consistent with the extremely high seismic attenuation observed beneath Cerro Galan by Liang et al. (submitted for publication) using the same dataset. Surface wave tomography studies from the same array further reveal pronounced low velocities in the crust in this area (Calixto et al., 2013). All of these observations imply that a zone of partial melt or a magma chamber exists in the crust beneath Cerro Galan as could result from the aftermath of lithospheric delamination. In accord with Kay et al. (1994, 2011), Bianchi et al. (2013) suggested that a delamination event in this area could have been triggered by pre-existing dense and thick crust. The region is also located in an area where a prominent Ordovician arc occurred (e.g., Rapela et al., 1992; Coira et al., 1999), which could have played a role in subsequent delamination. Thus, the thin mantle lithosphere with a depth of the LAB at 70–80 km (Fig. 10) could be interpreted as supporting a delamination model in this area.

Another region of high V_p/V_s is also observed south of the Puna plateau in the Pampean Ranges (see Fig. 6). No active volcanic edifice occurs in this region with the nearest center being the late Miocene Farallon Negro volcano to the west (see Fig. 1). The cause of the high V_p/V_s anomaly is still unclear.

In the upper mantle, the slab can be traced down to 170 km depth as is better seen on the migrated section in Fig. 11 where all available data are included (i.e. 300 km wide swath from 25°S to 28°S). Thus, Fig. 11 shows the complete geodynamic picture of the study area including the low-velocity zone in the crust, the Moho, the LAB, the subducting slab and the upper mantle discontinuities. In this profile, the mantle transition zone (MTZ) appears coincident with global averages elsewhere. In detail, the 410 km discontinuity is clear from 71°W to 66.5°W and then becomes less clear near the impingement of the slab and the MTZ in the east near 64°W. The 660 km is rather masked by noise but is partly identifiable in the west where it is at the expected global average depth. Finally, Fig. 11 is essential to demonstrate that the anomalous mantle transition zone suggested by Woelbern et al. (2009) to the north of the present array cannot be confirmed in this study.

5. Conclusions

The P and S receiver functions presented here provide for the first time an image of the crust and upper mantle in the southern Puna plateau. The crust is the thickest beneath the volcanic arc with a maximum depth of 75 km. In the southern Puna plateau the crustal thickness is 50–55 km. The thinnest crust occurs to the east of the plateau in the Sierras Pampeanas where the thickness is 35–40 km.

The crust of the plateau has a low V_p/V_s ratio (<1.7), implying a felsic crustal composition. The RF results revealed a widespread crustal low-velocity zone in the southern Puna plateau, consistent with the crustal low-velocity body observed by the teleseismic P wave tomography that occurs across the central part of the

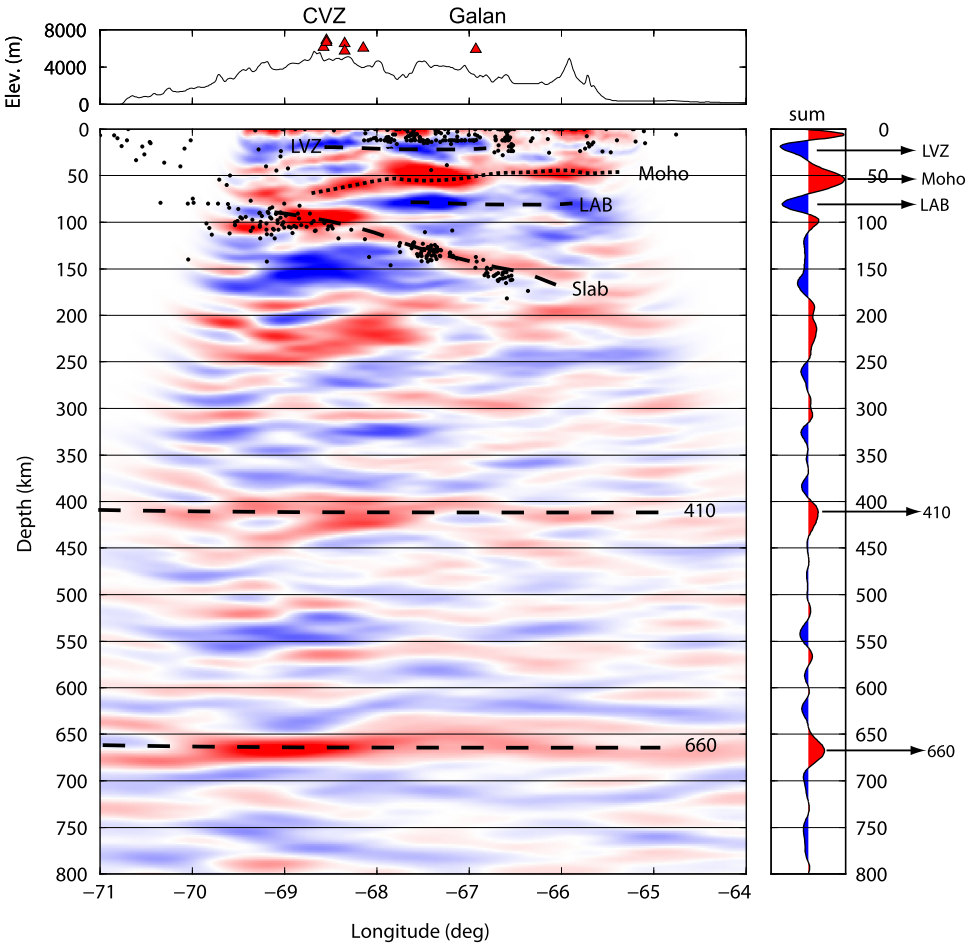

Fig. 11. Migrated upper mantle section along 27°S using data from all stations. Red and blue colors denote positive and negative amplitudes, respectively. The Moho in the Puna plateau (dotted line), as well as the LVZ, the LAB, the oceanic slab and the mantle transition zone discontinuities (dashed lines) can be well recognized in the figure. The CVZ (volcanic arc) and the Galan volcano are marked as a reference on the profile. On the right, the summation trace (sum) highlights the phases seen on the profile where it is possible to recognize that both 410 and 660 arrive at expected global averaged depths. (For interpretation of the references to color in this figure legend, the reader is referred to the web version of this article.)

southern Puna plateau and is related to various volcanic edifices (Bianchi et al., 2013). Such a widespread crustal low-velocity zone in the southern Puna is also in accord with surface wave (Calixto et al., 2013) and body wave attenuation (Liang et al., submitted for publication) tomographic images using teleseismic data and the earthquakes recorded in the study by Mulcahy et al. (submitted for publication).

A low-velocity crust with a high V_p/V_s ratio (1.87) observed beneath Cerro Galan provides evidence for a partial melt zone or magma chamber in the underlying crust that could have developed in the aftermath of lithospheric delamination. This hypothesis is in accord with the proposal of Kay et al. (1994, 2011) that the giant eruptions of the Cerro Galan ignimbrite complex were a consequence of delamination of the underlying crust and lithosphere, which triggered decompression melting in the underlying mantle wedge leading to extensive crustal melting.

The subducted Nazca plate has been clearly observed down to depths of 170 km in a region of transition between normal to flat subduction. The mantle transition zone discontinuities at 410 and 660 km appear at typical depths.

The receiver function images presented here are in accord with the continental lithospheric delamination events in this region suggested by previous authors (e.g., Kay et al., 1994; Bianchi et al., 2013). In detail, the PRF and SRF images reveal a relatively thin crust beneath the Puna plateau (50–60 km) compared to the Altiplano and the presence of a shallow LAB (70–90 km). Crustal thickening and eclogitization of the lower crust in response to crustal shortening and magmatic addition along with resteepening of a formerly shallower subduction zone (e.g., Kay and Coira, 2009) are consistent with the triggering of delamination events that left behind the thinned crust and shallow LAB now observed in the southern Puna.

Acknowledgements

We would like to thank the German Research Centre for Geosciences GFZ, the German Research Council (DFG) and the US National Science Foundation EAR Geophysics Grant (0538112) for the funding. The equipment has been provided by the Geophysical Instrument Pool Potsdam (GIPP), IRIS PASSCAL and the Universities of Missouri and St Louis. Waveform data are archived at the GEOFON and IRIS data centers. We thank the editor and two anonymous reviewers who helped to improve the manuscript.

References

Allmendinger, R.W., Jordan, T.E., Kay, S.M., Isacks, B., 1997. The evolution of the Altiplano–Puna Plateau of the Central Andes. Annu. Rev. Earth Planet. Sci. 25, 139–174.

Alvarado, P., Beck, S., Zandt, G., Araujo, M., Triep, E., 2005. Crustal deformation in the south-central Andes backarc terranes as viewed from regional broad-band seismic waveform modelling. Geophys. J. Int. 163, 580–598, http://dx.doi.org/10.1111/j.1365-246X.2005.02759.x.

Alvarado, P., Beck, S., Zandt, G., 2007. Crustal structure of the south-central Andes Cordillera and backarc region from regional waveform modelling. Geophys. J. Int. 170, 858–875, http://dx.doi.org/10.1111/j.1365-246X.2007.03452.x.

Ammon, C.J., 1990. On the nonuniqueness of receiver function inversions. J. Geophys. Res. 95, 2504–2510.

Angus, D.A., Wilson, D.C., Sandvol, E., Ni, J.F., 2006. Lithospheric structure of the Arabian and Eurasian collision zone in Eastern Turkey from S-wave receiver functions. Geophys. J. Int. 166 (3), 1335–1346.

Beck, S.L., Zandt, G., 2002. The nature of orogenic crust in the central Andes. J. Geophys. Res. 107 (B10), 2230, http://dx.doi.org/10.1029/2000JB000124.

Bianchi, M., Heit, B., Jakovlev, A., Yuan, X., Kay, S.M., Sandvol, E., Alonso, R., Coira, B., Brown, L., Kind, R., 2013. Teleseismic tomography of the southern Puna plateau in Argentina and adjacent regions. Tectonophysics 586, 65–83, http://dx.doi.org/10.1016/j.tecto.2012.11.016.

Cahill, T., Isacks, B., 1992. Seismicity and shape of the subducted Nazca plate. J. Geophys. Res. 97, 17503–17529.

Calixto, F.J., Sandvol, E., Kay, S., Mulcahy, P., Heit, B., Yuan, X., Coira, B., Comte, D., Alvarado, P., 2013. Velocity structure beneath the southern Puna plateau: Evidence for delamination. Geochem. Geophys. Geosyst., http://dx.doi.org/10.1002/ggge.20266.

Carbonell, R., Levander, A., Kind, R., 2013. The Mohorovičić discontinuity beneath the continental crust: an overview of seismic constraints. Tectonophysics. http://dx.doi.org/10.1016/j.tecto.2013.08.037.

Coira, B., Kay, S.M., Viramonte, J., 1993. Upper Cenozoic magmatic evolution of the Argentine Puna – A model for changing subduction geometry. Int. Geol. Rev. 35, 677–720.

Coira, B., Kay, S.M., Peréz, B., Woll, B., Hanning, M., Flores, P., 1999. Magmatic sources and tectonic setting of Gondwana margin Ordovician magmas, Northern Puna of Argentina and Chile. In: Ramos, V.A., Keppie, D. (Eds.), Laurentian–Gondwana Connections before Pangea. In: Spec. Pap., Geol. Soc. Am., vol. 336, pp. 145–170.

Dueker, K., Sheehan, A., 1997. Mantle discontinuity structure from midpoint stacks of converted to waves across the Yellowstone hotspot track. J. Geophys. Res. 102, http://dx.doi.org/10.1029/96JB03857.

Febrer, J.M., Baldis, B., Gasco, J.C., Mamani, M., Pomposielo, C., 1982. La anomalia geotermica Calchaqui en el noroeste de Argentina: un nuevo proceso geodinamico asociado a la subduccion de la placa de Nazca. In: Actas V Cong. Lat. Geol., vol. 3. Buenos Aires, pp. 691–703.

Fromm, R., Zandt, G., Beck, S.L., 2004. Crustal thickness beneath the Andes and Sierras Pampeanas at 30°S inferred from Pn apparent phase velocities. Geophys. Res. Lett. 31, http://dx.doi.org/10.1029/2003GL019231.

Gans, C.R., Beck, S.L., Zandt, G., Gilbert, H., Alvarado, P., Anderson, M., Linkimer, L., 2011. Continental and oceanic crustal structure of the Pampean flat-slab region, western Argentina, using receiver function analysis: new high-resolution results. Geophys. J. Int. 186, 45–58, http://dx.doi.org/10.1111/j.1365-246X.2011.05023.x.

Gilbert, H., Beck, S., Zandt, G., 2006. Lithospheric and upper mantle structure of central Chile and Argentina. Geophys. J. Int. 165, 383–398, http://dx.doi.org/10.1111/j.136546X.2006.02867.

Heit, B., 2005. Teleseismic tomographic images of the Central Andes at 21°S and 25.5°S: an inside look at the Altiplano and Puna plateaus. PhD thesis, Freie Universitaet Berlin, Scientific Technical Report (STR06/05). GeoForschungsZentrum, Potsdam, Germany.

Heit, B., Sodoudi, F., Yuan, X., Bianchi, M., Kind, R., 2007. An S-receiver function analysis of the lithospheric structure in South America. Geophys. Res. Lett. 34, L14307, http://dx.doi.org/10.1029/2007GL030317.

Heit, B., Koulakov, I., Asch, G., Yuan, X., Kind, R., Alcozer, I., Tawackoli, S., Wilke, H., 2008. More constraints to determine the seismic structure beneath the Central Andes at 21°S using teleseismic tomography analysis. J. South Am. Earth Sci. 25, 22–36.

Isacks, B.L., 1988. Uplift of the Central Andean Plateau and bending of the Bolivian Orocline. J. Geophys. Res. 93, 3211–3231.

Kay, S.M., Coira, B., 2009. Shallowing and steepening subduction zones, continental lithosphere loss, magmatism and crustal flow under the Central Andean Altiplano–Puna Plateau. In: Kay, S.M., Ramos, V.A., Dickinson, W.M. (Eds.), Backbone of the Americas: Shallow Subduction, Plateau and Ridge and Terrane Collisions. In: Mem. Geol. Soc. Lond., vol. 204, pp. 229–260.

Kay, R., Kay, S.M., 1993. Delamination and delamination magmatism. Tectonophysics 219, 177–189.

Kay, S.M., Mpodozis, C., 2002. Magmatism as a probe to the Neogene shallowing of the Nazca plate beneath the modern Chilean flatslab. J. South Am. Earth Sci. 15, 39–59.

Kay, S.M., Maksaev, V., Moscoso, R., Mpodozis, C., Nasi, C., 1987. Probing the evolving Andean lithosphere: Mid-late tertiary magmatism in Chile (29°–30°30S) over the modern zone of subhorizontal subduction. J. Geophys. Res. 92, http://dx.doi.org/10.1029/0JGREA0000920000B7006173000001.

Kay, S.M., Coira, B., Viramonte, J., 1994. Young mafic back arc volcanic rocks as indicator of continental lithospheric delamination beneath the Argentine Puna plateau, central Andes. J. Geophys. Res. 99, 24323–24339.

Kay, S.M., Mpodozis, C., Coira, B., 1999. Neogene magmatism, tectonism, and mineral deposits of the Central Andes (22° to 33° latitude). In: Skinner, B.J. (Ed.), Geology and Ore Deposits of the Central Andes, pp. 27–59. Society of Economic Geology Special Publication, vol. 7.

Kay, S.M., Coira, B., Wörner, G., Kay, R.W., Singer, B.S., 2011. Geochemical, isotopic and single crystal 40Ar/39Ar age constraints on the evolution of the Cerro Galán ignimbrites. Bull. Volcanol. 73, 1487–1511.

Kind, R., Kosarev, G.L., Petersen, N.V., 1995. Receiver functions at the stations of the German Regional Seismic Network (GRSN). Geophys. J. Int. 121, 191–202.

Kind, R., Yuan, X., Saul, J., Nelson, D., Sobolev, S.V., Mechie, J., Zhao, W., Kosarev, G., Ni, J., Achauer, U., Jiang, M., 2002. Seismic images of crust and upper mantle beneath Tibet: evidence for Eurasian plate subduction. Science 298, 1219–1221.

Kind, R., Yuan, X., Kumar, P., 2012. Seismic receiver functions and the lithosphere–asthenosphere boundary. Tectonophysics 536–537, 25–43, http://dx.doi.org/10.1016/j.tecto.2012.03.005.

Kley, J., Monaldi, C., 1998. Tectonic shortening and crustal thickness in the Central Andes: How good is correlation?. Geology 26, 723–726.

Kley, J., Monaldi, C.R., Salfity, J.A., 1999. Along-strike segmentation of the Andean foreland: Causes and consequences. Tectonophysics 301, 75–94.

Kumar, P., Yuan, X., Kind, R., Kosarev, G., 2005. The lithosphere–asthenosphere boundary in the Tien Shan–Karakoram region from S receiver functions – evidence for continental subduction. Geophys. Res. Lett. 32, L07305, http://dx.doi.org/10.1029/2004GL022291.

Kumar, P., Yuan, X., Kind, R., Ni, J., 2006. Imaging the colliding Indian and Asian continental lithospheric plates beneath Tibet. J. Geophys. Res. 111, B06308, http://dx.doi.org/10.1029/2005JB003930.

Li, X., Kind, R., Yuan, X., Wölbern, I., Hanka, W., 2004. Rejuvenation of the lithosphere by the Hawaiian plume. Nature 427, 827–829.

Liang, X., Sandvol, E., Kay, S.M., Heit, B., Yuan, X., Mulcahy, P., Chen, C., Brown, L.D., Comte, D., Alvarado, P., submitted for publication. Delamination of southern Puna lithosphere from body wave attenuation tomographic images. J. Geophys. Res.

Mulcahy, P., Chen, C., Kay, S.M., Brown, L.D., Isacks, B.L., Sandvol, E., Heit, B., Yuan, B., Coira, B.L., submitted for publication. Central Andean mantle and crustal seismicity under the Southern Puna plateau and Northern margin of the Chilean flatslab. Tectonics.

Oncken, O., Sobolev, S., Stiller, M., Asch, G., Haberland, C., Mechie, J., Yuan, X., Luechen, E., Giese, P., Wigger, P., Lueth, S., Scheuber, E., Götze, H.-J., Brasse, H., Buske, S., Yoon, M.-K., Shapiro, S., Rietbrock, A., Chong, G., Wilke, H.-G., Gonzales, G., Bravo, P., Vieytes, H., Martinez, E., Roessling, R., Ricaldi, E., 2003. Seismic imaging of a convergent continental margin and plateau in the central Andes (Andean Continental Research Project 1996 (ANCORP'96)). J. Geophys. Res. 108 (B7), 2328, http://dx.doi.org/10.1029/2002JB001771.

Porter, R., Gilbert, H., Zandt, G., Beck, S., Warren, L., Calkins, J., Alvarado, P., Anderson, M., 2012. Shear wave velocities in the Pampean flat-slab region from Rayleigh wave tomography: Implications for slab and upper mantle hydration. J. Geophys. Res. 117, B11301, http://dx.doi.org/10.1029/2012JB009350.

Rapela, C.W., Coira, B., Toselli, A., Saavedra, J., 1992. The Lower Paleozoic magmatism of Southwestern Gondwana and the evolution of Famatinian orogene. Int. Geol. Rev. 34, 1081–1142.

Sambridge, M., 1999. Geophysical inversion with a neighbourhood algorithm—I. Searching a parameter space. Geophys. J. Int. 138, 479–494.

Schneider, F.M., et al., 2013. Seismic imaging of subducting Eurasian continental lower crust beneath the Pamir. Earth Planet. Sci. Lett. 375, 101–112.

Sodoudi, F., Yuan, X., Liu, Q., Kind, R., Chen, J., 2006. Lithospheric thickness beneath the Dabie Shan, central eastern China from S receiver functions. Geophys. J. Int. 166, 1363–1367.

Ward, K., Porter, R.C., Zandt, G., Beck, S.L., Wagner, L.S., Minaya, E., Tavera, H., 2013. Ambient noise tomography across the Central Andes. Geophys. J. Int., http://dx.doi.org/10.1093/gji/ggt166.

Whitman, D., Isacks, B.L., Chatelain, J.-L., Chiu, J.-M., Perez, A., 1992. Attenuation of high-frequency seismic waves beneath the central Andean plateau. J. Geophys. Res. 97, 19929–19947.

Whitman, D., Isacks, B., Kay, S.M., 1996. Lithospheric structure and along-strike segmentation of the Central Andean Plateau; seismic Q. magmatism, flexure, topography and tectonics. Tectonophysics 259, 29–40.

Woelbern, I., Heit, B., Yuan, X., Asch, G., Kind, R., Viramonte, J., Tawackoli, S., Wilke, H., 2009. Receiver function images from the Moho and the slab beneath the Altiplano and Puna plateaus in the Central Andes. Geophys. J. Int. 177, 296–308.

Yuan, X., Ni, J., Kind, R., Mechie, J., Sandvol, E., 1997. Lithospheric and upper mantle structure of southern Tibet from a seismological passive source experiment. J. Geophys. Res. 102, 27491–27500.

Yuan, X., Sobolev, S.V., Kind, R., 2002. Moho topography in the central Andes and its geodynamic implications. Earth Planet. Sci. Lett. 199, 389–402.

Yuan, X., Kind, R., Li, X., Wang, R., 2006. The S receiver functions: synthetics and data example. Geophys. J. Int. 165, 555–564.

Zandt, G., Velasco, A., Beck, S., 1994. Composition and thickness of the southern Altiplano crust, Bolivia. Geology 22, 1003–1006.

Zhu, L., Kanamori, H., 2000. Moho depth variation in southern California from teleseismic receiver functions. J. Geophys. Res. 105, 2969–2980.